Rupture characteristics of the 2005 Tarapaca, northern Chile intermediate-depth earthquake: Evidence for heterogeneous fluid distribution across the subducting oceanic plate?

Keiko Kuge
Department of Geophysics, Kyoto University, Kyoto, 606-8502, Japan

Yuko Kase
Active Fault and Earthquake Research Center, National Institute of Advanced Industrial Science and Technology, AIST Tsukuba Central 7, Tsukuba, Ibaraki 305-8567, Japan

Yumi Urata
Department of Geophysics, Kyoto University, Kyoto, 606-8502, Japan

Jaime Campos and Adriana Perez
Department of Geophysics, University of Chile, Blanco Encalada 2002, Santiago, Chile

Abstract.

We examined the rupture of the 2005 Tarapaca, northern Chile earthquake at about 110 km depth with respect to both kinematic and dynamic characteristics, by using regional and teleseismic waveforms. The earthquake has a down-dip tensional focal mechanism. The subhorizontal rupture is characterized by two patches of large slip and high stress drop which are aligned nearly in the east-west direction, being perpendicular to the direction of the Chile Trench. Rupture initiated in the eastern patch, and then propagated to the western patch. Between the two patches, there exists a region of non-positive stress drop and high strength excess, which can cause sub-shear rupture to propagate from the eastern to the western patches but radiates little seismic waves. Seismic radiation energy from this earthquake tends to be low, which is consistent with the non-positive stress drop and high strength excess between the two patches. While the physical mechanism of intermediate-depth earthquakes is still controversial, current leading hypotheses are associated with dehydration within subducting plates. The rupture characteristics of the Tarapaca earthquake can be related to heterogeneous fluid distribution due to the dehydration. The spatial separation and dominant stress of the two large-slip patches agree with the characteristics of the previously reported double seismic zone beneath Chile. The two patches may be the manifestation of the double seismic zone where dehydration reactions can release fluid. Using a numerical simulation of 3-D dynamic rupture, we have shown that weakening due to fluid can account for the rupture characteristics of the Tarapaca earthquake.

1. Introduction

In subduction zones, many earthquakes occur at depths greater than 60 km where brittle failure of rocks cannot be generally explained because of the high pressure and temperature. Physical mechanisms of the earthquakes are controversial. Whereas transformation faulting associated with a meta-stable mantle phase is proposed for earthquakes deeper than 400 km, no similar transformation has been predicted at shallower depths [e.g. Kirby, 1995; Kirby et al., 1996]. Hypotheses for the physical mechanism of earthquakes at intermediate depths between 60 and 400 km include dehydration embrittlement of subducting hydrous rocks [e.g. Raleigh and Paterson, 1965] and viscous creep in fine-grained shear zones [Kelemen and Hirth, 2007]. Currently leading hypotheses are associated with dehydration. In laboratory experiments of antigorite dehydration, Dobson et al. [2002] observed strong acoustic emission signals and brittle deformation features associated with high pore-fluid pressure. Jung et al. [2004] showed, based on laboratory experiments, that faulting occurs in antigorite serpentine under high stress and their observations can be explained by separation of fluid from solid residue. In high velocity frictional experiments on natural serpentinite, Hirose and Bystricky [2007] observed dynamic weakening of the fault friction as a result of dehydration induced by frictional heating. Locations of earthquakes in subducting slabs appear to match the pressure-temperature condition of dehydration reactions [Hacker et al., 2003b; Yamasaki and Seno, 2003]. The existence of hydrous materials is supported by velocity structures in subducting plates which were determined from studies of seismic wave tomography [e.g., Tsuji et al., 2008; Dorbath et al., 2008; Nakajima et al., 2009a,b] and receiver functions [e.g. Kawakatsu and Watada, 2007]. On the other hand, there remain problems for dehydration-related hypotheses, which include ways water penetrates to deep portions of plates and uncertainties concerning dehydration reactions in the crust and mantle.

Source processes of intermediate-depth earthquakes have been examined, mainly in kinematic characteristics based on observations of seismic waves. Tibi et al. [2002] suggested that subevents of large intermediate-depth earthquakes tend to be located along the strike direction of subduction zones. Rupture directions of intermediate-depth earthquakes were systematically investigated by Warren et al. [2007] for the Tonga-Kermadec subduction zone and by Warren et al. [2008] for Middle America. The studies suggested that ruptures of many intermediate-depth earthquakes could propagate subhorizontally. In many previous studies including these, data were teleseismic waves recorded by global networks, but their resolution is limited. With better resolution of

regional data, Ide and Takeo [1996] showed, by constructing a dynamic source model, that subhorizontal rupture propagation of a large intermediate-depth earthquake (M_W 7.6) in Japan was controlled by the stress regime in the subducting slab.

A large intermediate-depth earthquake (M_W 7.8) occurred on 13 June 2005 at a depth of 115 km [National Earthquake Information Center (NEIC)] beneath Tarapaca in northern Chile. The Tarapaca earthquake is a rare event because of its large size and availability of regional data. For the period between 1976 and 2008, the Tarapaca earthquake is one of the three largest worldwide events in the depth range from 80 to 300 km. The aftershocks were located subhorizontally [Peyrat et al., 2006; Delouis and Legrand, 2007]. Seismic waves from the mainshock were recorded at regional distances by the seismic network of the University of Chile. The Tarapaca earthquake thus provides a good opportunity to understand what affects subhorizontal rupture of an intermediate-depth earthquake.

In this study, using regional and teleseismic waveform data, we determined kinematic and dynamic source models of the Tarapara earthquake. Seismic radiation energy was also examined. Based on these results, we discuss the rupture characteristics related to the physical mechanism of intermediate-depth earthquakes, with particular attention to implications for dehydration in a subducting slab.

2. Earthquake

In northern Chile, the Nazca plate subducts toward the east beneath the South American plate (Figure 1). In the subducting plate, down-dip tensional earthquakes occur at depths down to 350 km. The number of the earthquakes generally decreases with depth. Significant increase of earthquake activity, which deviates from the general trend, is observed at depths around 100-140 km. The Tarapaca earthquake in 2005 occurred in a consistent way with the earthquake activity in northern Chile. NEIC has reported no other large intermediate-depth earthquakes (M >7) in the Tarapaca region from 1976 to 2008, except for an event to the south in November, 1976 (20.52° S 68.92° W depth 82 km M 7.3).

There were several historical intermediate-depth earthquakes with magnitudes of about 7 to 8 in Chile during the twentieth century, for which down-dip tensional focal mechanisms were determined by waveform modeling techniques. The earthquakes include the 1939 Chillan, central Chile (M_S 7.8) [more than 20,000 people died; Beck et al., 1998] and 1950 Antofagasta, northern Chile (M_S 8.0) earthquakes [Kausel and Campos, 1992] as well as the smaller 1945 Santiago (M_S 7.1), 1965 La Ligua (M_S

7.1), 1965 Tal-tal (M_S 6.9), and 1970 Tocopilla (M_S 6.5) earthquakes [Malgrange et al. 1981; Leyton et al., 2009]. The down-dip tensional focal mechanisms were interpreted as rupturing along nearly vertical fault planes within the subducting plate. The clearly subhorizontal rupture of the 2005 Tarapaca earthquake raised a question whether or not some of these interpretations should be revisited.

The source characteristics of the 2005 Tarapaca earthquake were studied by Peyrat et al. [2006] (hereinafter referred to as P06) and Delouis and Legrand [2007] (hereinafter referred to as DL07). P06 located the aftershocks using data from a temporary seismic network deployed just after the mainshock. The aftershocks are distributed in a subhorizontal area being about 60 km long and 30 km wide. The slightly west dipping rectangular fault plane, which was also based on the point-source double couple mechanism obtained from teleseismic P and SH modeling, was consistent with observations of GPS and inSAR above the source region, and it was considered as an upper bound of the fault dimension. DL07 determined the slip distribution on subhorizontal faults in a simulated annealing scheme, by modeling teleseismic and regional waveforms simultaneously. The slip is concentrated in a region with 50 km length and 40 km width. Aftershocks relocated with their velocity model suggested that the slip extended to the west, overreaching the western boundary of the aftershock cluster. While they provided an overview of the slip distribution, the number of the model parameters and data were limited to carry out the simulated annealing technique. The shape of source time function at all grid points is fixed with a constant duration of 2 s. Resolution in the initial part of the rupture was reduced by their grid spacing (10 km), source duration, and search range of rupture times, which forced the first peak of the source time function to be isolated from the later moment release. The kinematic source characteristics of the Tarpaca earthquake are still worth examining by a different method under different conditions.

In both studies by P06 and DL07, the hypocenter of the mainshock was relocated using the regional permanent network of University of Chile, but the locations are different. The discrepancy could be attributed to differences of their velocity models and/or the arrival time data.

3. Waveform data

The Tarapaca earthquake was recorded within 300 km of the epicenter by five strong-motion acceleration seismometers, as shown in Figure 2. Figure 3 shows the displacement waveforms recorded at the station PICA above the source region. The

waveforms from the mainshock exhibit two significant pulses. Since the waveforms from an aftershock are characterized by a single pulse, the two pulses of the mainshock were not caused by wave propagation from the earthquake source to the station, and can be inferred to be two subevents during the rupture process.

The two subevents are also observed in the teleseismic P waveforms. Broadband waveform data at epicentral distances from 30 to 90 degree were retrieved from the archives of the Incorporated Research Institutions for Seismology Data Management Center (IRIS DMC). Figure 4a shows the teleseismic P and pP displacement waveforms as a function of station azimuth. The waveforms are generally simple, but we can see some variations of the waveform shape with azimuth. Two pulses are clearly observed in pP waves at stations to the east (e.g. ASCN, SHEL). Two pulses are also seen in P waves to the east (e.g. RCBR), although the directions for the direct P waves are close to a nodal plane of the P-wave radiation pattern. At stations to the east, the first pulse rises quickly, compared with the other stations, irrespective of P and pP. The peak of the P pulse is observed earlier at stations to the NNW direction. We cannot see an azimuthal variation of teleseismic S waveforms, probably due to attenuation.

4. Kinematic Source Model

4.1 Method

Using the regional and teleseismic waveform data, we determined a kinematic source model of the Tarapaca earthquake. Park and Mori [2008] showed that separate modeling of regional and teleseismic waveforms can provide good results where structure is complicated, for example, in a subduction zone. In their approach, several source models are first constructed by modeling teleseismic waveforms, and then the source models are evaluated by comparing their waveform fits at regional distances. In this study, we used their approach, modifying it for the Tarapaca earthquake. Considering that the observations of the two subevents are clear in the regional waveforms and are relatively weak in the teleseismic P waveforms, we first obtained several source models from regional waveforms, and then assessed the models by using teleseismic P and pP waveforms. A source model was derived from regional waveforms in two steps. In the first step, we determined a point-source moment tensor solution. Using the subhorizontal nodal plane for the fault plane, in the second step, we estimated spatiotemporal distribution of slip on a rectangular fault plane. The method is based on Kuge [2003].

The Tarapaca earthquake occurred in the subducting Nazca plate, and regional

seismic stations are distributed mainly in the north-south direction, as shown in Figure 2. It is possible that seismic waves are affected by the structure of the subducting high-velocity slab. Empirical Green function techniques could not be applied because records from small earthquakes were lacking. 3-D/2-D structure models have not been sufficiently developed to model regional waveforms, so testing the 3-D/2-D models is not realistic. On the other hand, uncertainties from 1-D velocity models can cause errors in modeling the regional waveforms. It is thus important to assess the robustness of the rupture characteristics.

For this purpose, we examined the stability of the characteristics of the kinematic source models, changing the 1-D velocity model and hypocenter. We tested three 1-D velocity models; the global model *iasp91* [Kennett and Engdahl, 1991] and the local models P06 and DL07. The velocity model of P06 has slower velocities than the others.

For estimating the spatiotemporal distribution of slip on a finite fault plane, the location of the hypocenter relative to the regional stations is important. We relocated hypocenters with the three velocity models, using arrival times of P and S waves that were read from the regional waveforms. Three different datasets of arrival times were tested in the relocation. The first dataset (5P5S) includes arrival times of P and S from all five stations in Figure 2. In the second dataset (5P3S), arrival times of S waves at CALA and TCP were excluded from the dataset 5P5S. The last dataset (3P3S) only includes arrival times of P and S from ARIE, IQUI, and PICA, which were used by DL07. For relocation with the last dataset, only the velocity model of DL07 was used because stable locations could not be obtained with the other velocity models. The relocated hypocenters are listed in Table 1. These hypocenters were used in our analysis of kinematic source models.

4.2 Point-source moment tensor solution

As shown in Figure 5, we obtained point-source moment tensor solutions from regional waveforms for seven sets of the velocity model and hypocenter. The moment tensor solutions do not depend sensitively on the choice of the velocity models and hypocenters. The focal mechanisms are characterized by down-dip tension, having nearly subvertical and subhorizontal nodal planes. Because the distribution of aftershocks was subhorizontal [P06, DL07], the subhorizontal nodal plane is likely to be the fault plane. Table 2 indicates the best double-couple parameters of the moment tensor solutions. They are in good agreement with the Global Centroid Moment Tensor (CMT) and other solutions [P06, DL07].

4.3 Spatiotemporal distribution of slip on a finite fault plane

On the fault planes determined by the point-source moment tensor solutions, we estimated the spatiotemporal distribution of slip. We determined amounts of slip on a square fault with length of 60 km, using the technique of multiple time windows [Hartzell and Heaton, 1983; Kuge, 2003], so that the shape of source time function can vary in this study. We used eight elements of a Herrmann function [Herrmann, 1979] with duration of 0.8 s in order to represent a source time function at each grid point on the fault. The spacing of grid points is 5 km. For the fault plane geometry and slip direction, we used the best double-couple parameters of our moment tensor solutions. We inverted three components of displacement waveforms.

Figure 6 shows the distributions of final slip for the seven sets of different velocity models and hypocenters. Two patches of large slip are observed in all the solutions. The patch near the hypocenter ruptured first. Between the patches, the amount of slip is small. The relative location of the two patches tends to be dependent on the velocity model and hypocenter. In most solutions, the two patches are aligned in an east-west to southeast-northwest direction, whereas they are located along the north-south direction in the solution based on the velocity model of P06. The solutions based on the velocity model of DL07 have slightly greater variance reduction, compared with the others, which means slightly better waveform modeling. The distributions of final slip obtained with the velocity model of DL07, irrespective of hypocenter location, are in good agreement with the one that DL07 determined only from regional waveforms.

In our multiple time-window inversions, a rupture-front velocity was tested in a range between 2 and 5 km/s. For all the seven cases in Figure 6, the sum of the squared residuals between observed and synthetic waveforms was minimized at rupture-front velocity of 3 to 3.5 km/s, which is about 70 % of the S-wave speed. Figure 7 shows snap shots of slip propagation from the kinematic source model obtained with the DL07 velocity model and 5P3S hypocenter. The distance between the two patches of large slip is about 20 km, and is larger than the typical thickness of oceanic crust. The total moment release is 5.4×10^{20} Nm, which is in good agreement with the values of the Global CMT solution, P06, and DL07. The average static stress drop is 33 MPa when we assume from Figure 7 that the rupture mainly occurred in a region of 40 km width and 20 km length. The waveform fit is shown in Figure 8.

4.4 Test against teleseismic P and pP waveforms

Using the spatiotemporal evolution of slip estimated on the finite fault, we computed synthetic waveforms of teleseismic P and pP, and compared them with observations. Synthetic waveforms are computed using the method of Wang [1999] with the global Earth model *iasp91*. We used the P and pP data shown in Figure 4. Several direct P waves propagating to the east were excluded because the directions are close to the nodal planes and the polarities are opposite in some source models. Instead, we used pP waves at stations to the east.

Table 3 gives correlation coefficients between the observed and synthetic waveforms. A large value means that the waveforms match better, and a value of 1.0 would indicate a perfect match. At each station, separate windows are used for P and pP waves, so that we can search the maximum value of correlation, shifting the time of each wave window independently. By using the separate time windows for P and pP, we can efficiently reduce effects of uncertainties from inexact local upper-mantle structure and source depth.

Figure 9 compares synthetic waveforms of the four source models with correlation coefficients 0.92 or greater. All source models can explain P waveforms well. Two pulses of the pP waves can be successfully modeled by synthetic waveforms of the source models obtained with the velocity model of DL07, whereas the second pulse does not appear strongly in the synthetic waveforms of the P06 model.

This difference in the synthetic pP waveforms is caused by the different locations of the two patches. As shown in Figure 6, the two patches of large slip are aligned in the north-south direction in the P06 model, but they are in an east-west to southeast-northwest direction in all the DL07 models. The two pulses of the observed pP waveforms thus require that the two patches of large slip be located nearly in the east-west direction. This suggests that the subhorizontal rupture of the Tarapaca earthquake crossed the subducting plate, propagating from the hypocenter bilaterally toward the surface and deeper into the plate.

Synthetic waveforms of P and pP computed from the kinematic source model using the DL07 velocity model and the 5P3S hypocenter for other station azimuths are shown in Figure 4b.

We also carried out our kinematic studies with regional and teleseismic data in the same way, assuming S-wave speed rupture propagation. We had no evidence supporting the fast rupture propagation, although rupture velocity is often difficult to determine [Park and Mori, 2008].

5. Seismic radiation energy

We computed seismic radiation energy from the Tarapaca earthquake using the method of Venkataraman and Kanamori [2004b]. We used teleseismic P waves recorded at global broadband stations of IRIS. Only vertical components were used. Seismic energy was estimated from the spectrum at each station. Geometrical spreading factor, free surface receiver effect, and instrumental response were corrected in the frequency domain. The value of t^* was assumed to be 1 s. P-wave energy was summed up in frequencies up to 1 Hz in the same way as Venkataraman and Kanamori [2004b]. The total seismic energy was computed from the P-wave energy, using the S-to-P wave energy ratio estimated from P- and S-wave speeds [Venkataraman and Kanamori, 2004a]. We verified our procedure by using the 1993 Kushiro, northern Japan, earthquake (M_W 7.6, depth 100 km) and found that our estimate of seismic radiation energy (4.5×10^{16} J) is close to the value (4.3×10^{16} J) of Venkataraman and Kanamori [2004b].

The values of seismic radiation energy (E_r) from the Tarapaca earthquake are shown in Figure 10, in comparison with the Kushiro earthquake. The values do not vary with azimuth, so the directivity effect, which was discussed by Venkataraman and Kanamori [2004a], is negligible. The average value of the Tarapaca earthquake is $2.2\times10^{16}\pm0.3\times10^{16}$ J. With the seismic moment (M_o) of 5.4×10^{20} Nm, the energy-to-moment ratio (E_r / M_o) is 4.1×10^{-5}. These values are lower than those of the Kushiro earthquake. Radiation efficiency of the Tarapaca earthquake is estimated to be 0.2 for the average static stress drop of 33 MPa. This is also a relatively small value.

Estimates of seismic radiation energy depend on the choice of t^*. The value that we used is close to the average value from PREM for teleseismic P waves [Dziewonski and Anderson, 1981]. If t^* is larger, the estimate of seismic radiation energy is increased. The seismic radiation energy of the Tarapaca earthquake is about a half of that of the Kushiro earthquake. If this difference is completely attributed to the difference of t^* associated with P waves from the Tarapaca earthquake, the average value of t^* should be 1.25 s. The P-wave attenuation structure beneath South America has not been determined because of insufficient data [e.g. Warren and Shearer, 2002], so it is unclear whether or not the mantle beneath northern Chile can account for the larger t^*, compared to northern Japan.

6. Dynamic source model

From the obtained kinematic source model, we inferred dynamic source parameters following Mikumo and Miyatake [1993] and Mikumo et al. [1998]. The rectangular fault plane shown in Figure 6 was divided into square subfaults with the size of 5 km. Assuming a slip-weakening relation (Figure 11a), we determined values of strength excess and dynamic stress drop for each subfault. Dynamic stress drop is set to be positive when dynamic friction is smaller than initial stress, and negative stress drop was also allowed in this study. Initial stress was assumed to be uniform over the fault. The critical distance (D_c) was assumed to be 1 m. The amounts of slip and rupture times in the subfaults were given by our kinematic source model. We iteratively modeled them by modifying values of strength excess and dynamic stress drop in the subfaults, computing 3-D spontaneous dynamic rupture with the modified values, and comparing the dynamic rupture process with our kinematic source model. We used the kinematic source model obtained from the DL07 velocity model and 5P3S hypocenter. Dynamic ruptures were computed in the finite-difference method based on Kase and Kuge [2001].

Figure 11 shows the distributions of strength excess and dynamic stress drop. Two patches of high, positive stress drop are clearly observed. The two patches are located in the east-west direction, which correspond to the two patches of large slip in the kinematic source model. At the edges of the two patches, high values of strength excess are observed, which control the sizes of the large slip regions.

Between the two patches of high, positive stress drop, there exists a region of negative stress drop and high strength excess, which is not due to artificial errors from the determination process. In our kinematic source model, the rupture in the western patch is delayed compared with that in the eastern patch (Figure 7), and the amount of slip between the two patches is small. The delay and small slip require negative stress drop and high strength excess in the region between the hypocenter and the western patch. Stress drop in the region between the two patches may be zero but not positive. We also tested the non-negative stress drop constraint in the determination process. The obtained distributions of strength excess and dynamic stress drop, which fit well to the kinematic source model and observed waveforms, are similar to those of the dynamic source model without the constraint, except that the region with negative stress drop shown in Figure 11c has almost zero stress-drop.

Positive stress drop releases strain energy, whereas regions of non-positive stress drop

need energy for rupture propagation. From our dynamic source model shown in Figure 11, we compared the incoming and outgoing energy on the fault. Stress drop $\Delta\boldsymbol{\tau}$ and final slip amount $\Delta\mathbf{u}$ are available in each subfault. We computed the inner product ($\Delta\boldsymbol{\tau}\cdot\Delta\mathbf{u}$) in each subfault, and summed them for the regions of negative and positive values, separately. The sum in the region of negative stress drop is about 8 % of that in the region of positive stress drop. Although these values are not complete energy estimates, it is implied that a considerable amount of energy could be consumed in the region of negative stress drop, which may be consistent with the observation of low seismic radiation energy from the Tarapaca earthquake.

When D_c was half the value (i.e. 0.5 m), we observed that the spatial patterns of strength excess and stress drop are similar to those in Figure 11. The values of strength excess become larger, almost double at the peaks, whereas the values of stress drop do not change significantly. The larger values of strength excess can be due to increase in stress concentration just ahead of rupture fronts, because the smaller D_c causes a more rapid rise of slip velocity function. Stress drop mainly depends on amount of slip, which can accounts for the small variation with D_c.

Since there exist trade-offs between some dynamic source parameters [e.g., Guatteri and Spudich, 2000; Peyrat et al., 2004], our dynamic source model is non-unique. We assumed that D_c is uniform over the fault, but large values of D_c can provide an alternate explanation for the negative stress drop. Large values of D_c need large energy for rupture front propagation, and behave in a similar way to negative stress drop.

We also assumed that the initial stress is uniform over the fault. If spatial variation of initial stress on the fault is responsible for the characteristics of the kinematic source model, the initial stress would be high on the two patches, whereas the initial stress between the patches would be lower than the dynamic friction stress. In this situation, the high initial stress on the two patches needs to be explained as well.

Figure 12 shows snap shots of the slip propagation obtained from the dynamic source model. The large slip spreading over the two patches is similar to the results of the kinematic source model. The two patches of final slip are in agreement with each other for the kinematic and dynamic models. Figure 8 shows the synthetic waveforms computed from the dynamic source model, as well as the kinematic source model. Although the synthetic waveform fit is not as good as for the kinematic source model, as is generally predicted, predominant features in the observed waveforms are successfully modeled by the dynamic source model.

Assuming that the rupture is represented by two ellipse asperities, Peyrat and Favreau

[2010] built kinematic and dynamic source models from regional waveforms using a different technique from ours. Our models agree with theirs about the two dominant patches of high slip, the positive and negative pattern of stress drop, and the second patch located in a deep portion of the slab. There are differences in the geometry of the two patches including the sizes, distance, and azimuth. Their large patches and long distance between the two patches could be attributed to the S-wave speed rupture propagation. There is, however, no evidence supporting the fast rupture propagation in our kinematic studies with regional and teleseismic data.

Finally, Figure 13a summaries the rupture characteristics of the Tarapaca earthquake, based on our studies of the kinematic and dynamic source models along with the seismic radiation energy.

7. Discussion

7.1. Dehydration, intermediate-depth seismicity, and double seismic zone

Earthquakes associated with a subduction zone mainly occur near the subducting plate surface and within the subducting plate, and the seismicity often consists of two bands at intermediate depths [e.g. Hasegawa et al. 1978], which forms a “double seismic zone”. What causes double seismic zones is an outstanding question for intermediate-depth earthquakes. In dehydration-related hypotheses, two bands of the double seismic zone correspond to dehydration reactions of hydrous materials in crust and mantle [Hacker et al., 2003b; Yamasaki and Seno, 2003].

Beneath northeastern Japan, a clear double seismic zone is observed [e.g., Hasegawa et al., 1978]. Based on data from the dense seismic networks in Japan, the nature of the seismicity and slab structure has been discussed in the framework of the dehydration-related hypotheses by many researchers.

The focal mechanisms in the upper band of the double seismic zone are predominantly down-dip compressional, whereas they are down-dip tensional in the lower band [e.g., Hasegawa et al., 1978]. There are several clusters of earthquakes at depths around 70-100 km in the upper band. Kita et al. [2006] proposed that the clusters are located in the oceanic crust, which was observed as a low-velocity layer in the seismic wave tomography [Tsuji et al., 2008]. The relocated hypocenters also display a specific distribution in the low-velocity layer, which can be explained by a dehydration reaction from blueschist to eclogite, as was predicted by Hacker et al. [2003a]. Seismic wave tomography [Nakajima et al., 2009a] found that the low-velocity layer becomes

deeper in a region where temperature is lower, as is predicted by the dehydration reaction of Mid-ocean Ridge Basalts (MORB) [Hacker et al., 2003a]. These observations support the notion that earthquake clusters at depths around 100 km can be associated with dehydration of subducting oceanic crust. On the other hand, it is suggested that earthquake locations in the lower band of the double seismic zone may be the dehydration locus of mantle material [e.g. Peacock, 2001; Hacker et al., 2003b; Yamasaki and Seno, 2003].

Observations in northern Chile also support the notion that intermediate-depth earthquakes can be associated with dehydration reactions in the subducting slab, although the Tarapaca source region has not been directly studied.

Earthquakes beneath northern Chile predominantly occur in the low-velocity oceanic crust at depths between 70 and 210 km, which was suggested by studies of converted phases [Bock et al., 2000] and receiver functions [Yuan et al., 2000]. Double seismic zones are observed in some regions beneath northern Chile [e.g. Comte and Suarez, 1994; Comte et al., 1999; Rietbrock and Waldhauser, 2004; Dorbath et al., 2008]. North (18°S−19°S) of the Tarapaca region, two seismic bands with a thickness of 5 to 10 km and a separation of 20 km, are delineated between 80 and 140 km depth [Comte et al., 1999; Dorbath et al. 2008]. P- and S-wave speeds and their ratio on and between the two bands, which were determined by a seismic tomography technique [Dorbath et al., 2008], imply the possible existence of hydrous materials on the two bands. The pressure-temperature conditions met by the locations of the two bands also agree with the dehydration reaction [Dorbath et al., 2008]. The focal mechanisms of earthquakes on both bands exhibit wide variability [Comte et al., 1999; Dorbath et al. 2008]. South (20°S−24°S) of the Tarapaca region, the characteristics of double seismic zones seem to be controversial, and may vary from place to place. Comte and Suarez [1994] observed two families of earthquakes with opposite focal mechanisms, suggesting a double seismic zone with a separation of about 15 km. In the same region, however, Graeber and Asch [1999] gave no evidence for a double seismic zone. On the other hand, in the region around 22°S, high-precision earthquake relocations with data from recent temporary seismic observations provided a very clear image of a double seismic zone at depths between 80 and 130 km [Rietbrock and Waldhauser, 2004]. The upper and lower bands of the double seismic zone are separated by about 9 km, which corresponds to a horizontal distance of about 20 km. In both bands, down-dip tensional faulting is predominant. It should be noted here that this characteristic of the double seismic zone is in good agreement with the characteristics of the two large-slip patches found for the 2005 Tarapaca earthquake. The thermal model of Wada and Wang [2009] around

23.5°S predicts that a hydrated region in the crust extends to about 100 km depth and a zone of antigorite stability exists below the crust.

7.2. Possible effect of fluid on earthquake rupture

Dehydration releases water from hydrated rocks. One of the predicted effects is that the released water increases pore pressure in rocks, decreasing effective normal stress, and allowing faulting to occur under high pressure.

In addition to increase of pore pressure due to increased fluid volume, thermal pressurization is predicted to occur during faulting of rocks with low permeability. Sibson [1977] proposed this as one possible effect of fluid, in which increase in pore fluid pressure, due to frictional heating under wet conditions, further reduces effective normal stress.

These changes of pore pressure can affect earthquake ruptures, and the influence can appear in relations between shear stress and slip on faults. Figure 14 illustrates predicted effects of pore pressure on a slip-weakening relation. When the constant part of pore pressure, p_0, decreases effective normal stress, strength excess is decreased, and stress drop is increased. Additionally, when thermal pressurization occurs as the result of frictional heating, the stress drop is further increased, but strength excess is unchanged. Combinations of these pore-pressure changes can yield variations in strength excess and stress drop on a fault, encouraging growth and propagation of rupture.

When dehydration occurs in a subducting plate, released fluid is likely to be distributed heterogeneously because dehydration reaction is governed by the pressure-temperature condition. If a double seismic zone is the manifestation of dehydration, fluids can be expected along the two bands of the double-seismic zones, whereas there are no fluids in the other regions. As a result, increases in pore pressure can act along the two bands of double-seismic zones, while no effects of pore pressure change can be expected in the other regions.

The rupture characteristics of the Tarapaca earthquake may be connected with the idea of heterogeneous fluid distribution associated with dehydration. Figure 15 shows a numerical simulation of 3-D spontaneous dynamic rupture including pore pressure with thermal pressurization. We computed dynamic rupture propagation on a rectangular fault using the method of Urata et al. [2008]. A slip-weakening relation was assumed, and the friction coefficients were set to produce negative stress drop uniformly over the fault. The initial stress was also uniform. The rectangular fault is divided into three regions. Fluid exists in the two regions at the edges, and there is no fluid between the

two regions. The two regions with fluid are the imitation of a double seismic zone. The background pore pressure is set to be zero in this simulation because its effect is easily predicted as a constant variation in strength excess and stress drop (Figure 14) and the value of strength excess is nearly uniform in our dynamic source model (Figure 11), except for the periphery region. Once slip is initiated, the stress drop becomes positive in regions with fluid, due to thermal pressurization, causing large slip. Stress drop is continuously negative in the region without fluid, where rupture propagates but slip is very small. Although the frictional coefficients and initial stress were uniform over the fault, we can see regions of positive and negative stress drop, depending on whether or not fluid exists. The regions of positive and negative stress drop also correspond to regions of large and small slip, respectively. The dynamic rupture shown in Figure 15 looks similar to the rupture characteristics observed for the Tarapaca earthquake.

Figure 13b illustrates an idea proposed for the Tarapaca earthquake. Two patches of large slip and high stress drop were observed for the Tarapaca earthquake, and the distance between the two patches agrees with the separation between the upper and lower bands of the double-seismic zone observed in the south [Rietbrock and Waldhauser, 2004]. Predominant down-dip tension found in both bands of the double-seismic zone explains the focal mechanisms of the two patches. These imply that the two patches can be a part of a double-seismic zone where fluid exists from dehydration. Large slip and stress drop in the two patches may be the result of weakening due to fluid, whereas non-positive stress drop and high strength excess between the two patches may reflect an area of no fluids.

We have discussed the effect of dehydration in subducting plates, based on pore pressure with thermal pressurization. It is to be noted, however, that pore pressure and thermal pressurization can be replaced with other possible processes of weakening due to fluids or dehydration reactions. Similar characteristics of dynamic rupture, as shown in Figure 15, can be produced by other weakening processes, if they exist. Recent frictional experiments with hydrous rocks provided observations for weakening of frictional strength associated with dehydration. Takahashi et al. [2009] showed that frictional strength weakens due to dehydration in increasing temperature. In high velocity friction experiments, Hirose and Bystricky [2007] observed dynamic weakening of the fault friction as a result of dehydration induced by frictional heating. Further studies from these experiments are important.

Our interpretation of the role of fluids in the double seismic zone can provide a good explanation for observations for the Tarapaca earthquake. On the other hand, it has uncertainties due to unsolved problems. The problems include, what are the fault

constitutive relations of dry and hydrated slab materials under high stress, what characteristics of a double seismic zone are in the Tarapaca source region, and where are exact locations of the plate surface, subducting crust, and double seismic zone relative to the detected two patches. These problems should be investigated in the future in order to test the interpretation further.

7.3 Comparison to the 1993 Kushiro, Japan, earthquake

An earthquake apparently similar to the 2005 Tarapaca earthquake occurred in 1993 at the depth of 100 km beneath Kushiro in northern Japan, with a magnitude of M_W 7.6. The focal mechanism is down-dip tensional, having subhorizontal and subvertical nodal planes. The subhorizontal distribution of aftershocks suggests that the fault plane was subhorizontal.

Using regional strong-motion waveforms in Japan, the dynamic rupture parameters of the Kushiro earthquake were determined by Ide and Takeo [1996]. The comparison with the background seismicity showed that the rupture of the Kushiro earthquake initiated in the lower band of the double-seismic zone. The rupture continuously expanded, causing a narrow region of large slip and high stress drop in the neighborhood of the lower band toward the upper band. The region dominantly extended along the strike direction of the Kurile subduction zone. High strength excess was found along the edge of the large-slip region on the side toward the upper band, which stopped the rupture before it reached the upper band. The high strength excess was inferred from the polarity change of stress within the plate, from predominantly down-dip tension in the lower band to predominantly down-dip compression in the upper band, for the double seismic zone beneath northern Japan.

The different stress regimes between northern Chile and Japan could cause the different patterns of rupture propagation of large earthquakes in the double seismic zones. Beneath northern Chile, down-dip tensional earthquakes are predominant (Figure 1). In some regions, dominant down-dip tension is clearly suggested in both bands of the double-seismic zone [Rietbrock and Waldhauser, 2004]. Such a stress regime in the subducting slab could allow subhorizontal rupture, such as the Tarapaca earthquake, to propagate in a wide region across the subducting plate. As a result, the rupture could produce two regions of large slip, which correspond to a double seismic zone, with a region of non-positive stress drop and high strength excess between, which has low seismic radiation. On the other hand, the rupture of the Kushiro earthquake could not propagate across a wide region of the slab because of opposite stress polarities in the

two bands of the double seismic zone. For this case, there are not either two patches of large slip across the slab or low levels of seismic radiation energy.

Along the lower band of the double seismic zone beneath Kushiro, low P-wave velocity anomalies are observed in the seismic wave tomography images of Nakajima et al. [2009b]. The images also suggested that a local region of low P-wave velocity extends from the lower band, subhorizontally toward the upper band, corresponding to the aftershock area of the Kushiro earthquake. The rupture of the Kushiro earthquake, which started in the lower band, could continuously propagate along the region in and around the lower band.

Some numerical computations for the stress field within a subducting plate predict that a region of compressional stress exists between two bands under tensional stress, due to unbending [Wang, 2002] and compressional stress transferred from a thick continental lithosphere [Dorbath et al., 2008]. One of the bands under tensional stress corresponds to subducting crust, while the other band is located in mantle. The rupture characteristics of the Tarapaca earthquake imply that the compressional stress can be very weak if it exists. The state of the stress in the subducting Nazca plate is apparently dominated by the effect of slab pull.

8. Conclusions

The kinematic and dynamic rupture characteristics of the 2005 Tarapaca, northern Chile earthquake at depth of about 110 km were examined by using regional and teleseismic waveforms. The earthquake has a down-dip tensional focal mechanism, and the fault plane is inferred to be subhorizontal, based on the previous reports of the aftershock distribution. The subhorizontal rupture is characterized by two patches of large slip and high stress drop. The two patches are aligned nearly in an east-west direction, being perpendicular to the strike direction of the Chile Trench. Rupture initiated in the eastern patch, and then propagated to the western patch. Between the two patches, there exists a region of non-positive stress drop and high strength excess, which can cause sub-shear rupture to propagate from the first to the second patches but radiates little seismic waves. The seismic radiation energy from the Tarapaca earthquake tends to be low, which is consistent with the existence of the region of non-positive stress drop and high strength excess between the two patches.

Whereas the physical mechanism of intermediate-depth earthquakes is still under debate, observations, which can provide tests for the hypothesis that the earthquakes are associated with dehydration in subducting oceanic plates, are increasing. We propose

that the rupture characteristics observed for the Tarapaca earthquake may be associated with heterogeneous fluid distribution due to dehydration within the plate. The spatial separation and dominant stress of the two large-slip patches are consistent with the characteristics of the previously reported double seismic zone. The two patches may be the manifestation of a double seismic zone where dehydration reactions can release fluid. We have shown that a numerical simulation of 3-D dynamic rupture, including the effect of weakening due to thermal pressurization, can account for the rupture characteristics of the Tarapaca earthquake. Some assumptions made in the numerical simulations (e.g. fault constitutive relations of dry and hydrated rocks in the slab) are yet to be validated with, for example, laboratory experiments.

The structure and earthquake genesis within subducting oceanic plates have been examined mainly from seismicity and velocity structure. The present study of the Tarapaca earthquake demonstrates that rupture characteristics of a large intermediate-depth earthquake can also provide information for understanding the deformation/faulting properties within a plate. In particular, earthquakes beneath northern Chile are ideal for this purpose because both bands of the double seismic zone appear to be under stress of the same polarity. This situation allows rupture of a large earthquake to propagate across a wide region of the subducting slab involving both bands.

Acknowledgments.
We would like to thank the LIA M. de Ballore (CNRS - U. de Chile collaboration) and the Millennium Nucleus CIIT-MB Mideplam-Chile Program. We also greatly thank the personnel of the IRIS network. We used GMT (Generic Mapping Tool version 4.1.4, Wessel and Smith [1998]) for drawing some figures. Jim Mori helped to improve the manuscript. We thank Associate Editor Kelin Wang and two anonymous reviewers for helpful comments on the manuscript.

References

Beck, S., S. Barrientos, E. Kausel, and M. Reyes (1998), Source characteristics of historic earthquakes along the central Chile subduction zone, *J. South American Earth Sciences, 11*, 115-129.

Bizzarri, A., and M. Cocco (2006), A thermal pressurization model for the spontaneous dynamic rupture propagation on a three-dimensional fault: 1. Methodological approach, *J. Geophys. Res.*, *111*, B05303, doi:10.1029/2005JB003862.

Bock, G., B. Schurr, and G. Asch (2000), High-resolution image of the oceanic Moho in the subducting Nazca plate from P-S converted waves, *Geophys. Res. Lett., 27*, 3929-3932.

Comte, D. and G. Suarez (1994), An inverted double seismic zone in Chile: Evidence of phase transformation in the subducted slab, *Science, 263*, 212-215.

Comte, D., L. Dorbath, M. Pardo, T. Monfret, H. Haessler, L. Rivera, M. Frogneux, B. Glass, and C. Meneses (1999), A double-layered seismic zone in Arica, northern Chile, *Geophys. Res. Lett., 26*, 1965-1968.

DeMets, C., R. G. Gordon, D. F. Argus, and S. Stein (1994), Effect of recent revisions to the geomagnetic reversal time scale on estimates of current plate motions, *Geophys. Res. Lett., 21*, 2191-2194.

Delouis, B. and D. Legrand (2007), M_W 7.8 Tarapaca intermediate depth earthquake of 13 June 2005 (northern Chile): Fault plane identification and slip distribution by waveform inversion, *Geophys. Res. Lett., 34*, L01304, doi:10.1029/2006GL028193.

Dobson, D. P., P. G. Meredith, and S. A. Boon (2002), Simulation of subduction zone seismicity by dehydration of serpentine, *Science, 298*, 1407-1410.

Dorbath, C., M. Gerbault, G. Carlier, and M. Guiraud (2008), Double seismic zone of the Nazca plate in northern Chile: High-resolution velocity structure, petrological implications, and thermomechanical modeling, *G3, 9*, Q07006, doi:10.1029/2008GC002020.

Dziewonski, A. M., and D. L. Anderson (1981), Preliminary reference Earth model, P*hys. Earth Planet. Inter., 25*, 297-356.

Graeber, F. M., and G. Asch (1999), Three-dimensional models of P wave velocity and P-to-S velocity ratio in the southern central Andes by simultaneous inversion of local earthquake data, *J. Geophys. Res., 104* (B9), 20237-20256, doi:10.1029/1999JB900037.

Guatteri, M., and P. Spudich (2000), What can strong-motion data tell us about

slip-weakening fault-friction laws? , *Bull. Seismo. Soc. Amer., 90*, 98-116.

Hacker, B. R., G. A. Abers, and S. M. Peacock (2003a), Subduction factory 1. Theoretical mineralogy, densities, seismic wave speeds, and H2O contents, *J. Geophys. Res., 108 (B1)*, 2029, doi:10.1029/2001JB001127.

Hacker, B. R., S. M. Peacock, G. A. Abers, and S. D. Holloway (2003b), Subduction factory 2. Are intermediate-depth earthquakes in subducting slabs linked to metamorphic dehydration reactions?, *J. Geophys. Res., 108 (B1)*, 2030, doi:10.1029/2001JB001129.

Hartzell, S. H. and T. H. Heaton (1983), Inversion of strong ground motion and teleseismic waveform data for the fault rupture history of the 1979 Imperial Valley, California, earthquake, *Bull. Seismo. Soc. Amer., 73*, 1553-1583.

Hasegawa, A., N. Umino, and A. Takagi (1978), Double-planed structure of the deep seismic zone in the northeastern Japan Arc, *Tectonophysics, 47*, 43-58.

Herrmann, R. B. (1979), SH-wave generation by dislocation sources – a numerical study, *Bull. Seism. Soc. Am., 69*, 1-15.

Hirose, T., and M. Bystricky (2007), Extreme dynamic weakening of faults during dehydration by coseismic shear heating, *Geophy. Res. Lett., 34*, L14311, doi:10.1029/2007GL030049.

Ide, S., and M. Takeo (1996), The dynamic rupture process of the 1993 Kushiro-oki earthquake, *J. Geophys. Res., 101 (B3)*, 5661-5675.

Jung, H., H. W. Green II, and L. F. Dobrzhinetskaya (2004), Intermediate-depth earthquake faulting by dehydration embrittlement with negative volume change, *Nature, 428*, 545-549.

Kase, Y. and K. Kuge (2001), Rupture propagation beyond fault discontinuities: significance of fault strike and location, *Geophys. J. Int., 147*, 330-342.

Kausel, E., and J. Campo (1992), The Ms=8 tensional earthquake of 9 December 1950 of northern Chile and its relation to the seismic potential of the region, *Phys. Earth. Planet. Int., 72*, 220-235.

Kawakatsu, H., and S. Watada (2007), Seismic evidence for deep-water transportation in the mantle, *Science, 316*, 1468-1471, doi:10.1126/science.1140855.

Kelemen, P. B. and G. Hirth (2007), A periodic shear-heating mechanism for intermediate-depth earthquakes in the mantle, *Nature, 446*, 787-790, doi:10.1038/nature05717.

Kennett, B. L. N., and E. R. Engdahl (1991), Traveltimes for global earthquake location and phase identification, *Geophys. J. Inter., 105*, 429-465.

Kikuchi, M., and M. Ishida (1993), Source retrieval for deep local earthquakes with

broadband records, *Bull. Seismo. Soc. Amer., 83*, 1855-1870.

Kirby, S. (1995), Interslab earthquakes and phase changes in subducting lithosphere, *Rev. Geophysics, 33*(S1), 287-297.

Kirby, S., E. R. Engdahl, and R. Denlinger (1996), Intermediate-depth intraslab earthquakes and arc volcanism as physical expressions of crustal and uppermost mantle metamorphism in subducting slabs, in *Subduction: Top to Bottom* (edited by G. E. Bebout et al.), pp. 195-214, American Geophysical Union.

Kita, S., T. Okada, J. Nakajima, T. Matsuzawa, and A. Hasegawa (2006), Existence of a seismic belt in the upper plane of the double seismic zone extending in the along-arc direction at depths of 70-100 km beneath NE Japan, *Geophys. Res. Lett., 33*, L24310, doi:10.1029/2006GL028239.

Kuge, K. (2003), Source modeling using strong-motion waveforms: Toward automated determination of earthquake fault planes and moment-release distributions, *Bull. Seismo. Soc. Amer., 93*, 639-654.

Leyton, F., J. Ruiz, J. Campos, and E. Kausel (2009), Intraplate and interplate earthquakes in Chilean subduction zone: A theoretical and observational comparison, *Phys. Earth Planet. Inter., 175*, 37-46,

Malgrange, M., A. Deschamps, and R. Madariaga (1981), Thrust and extensional faulting under the Chilean coast: 1965, 1971 Aconcagua earthquakes, *Geophys. J. R. Astron. Soc., 66*, 313–331.

Mikumo, T. and T. Miyatake (1993), Dynamic rupture processes on a dipping fault, and estimates of stress drop and strength excess from the results of waveform inversion, *Geophys. J. Inter., 112*, 481-496.

Mikumo, T., T. Miyatake, and M. A. Santoyo (1998), Dynamic rupture of asperities and stress change during a sequence of large interplate earthquakes in the Mexican subduction zone, *Bull. Seismo. Soc. Amer., 88*, 686-702.

Nakajima J., Y. Tsuji, and A. Hasegawa (2009a), Seismic evidence for thermally-controlled dehydration reaction in subducting oceanic crust, *Geophys. Res. Lett., 36*, L03303, doi:10.1029/2008GL036865.

Nakajima, J., Y. Tsuji, A. Hasegawa, S. Kita, T. Okada, and T. Matsuzawa (2009b), Tomographic imaging of hydrated crust and mantle in the subducting Pacific slab beneath Hokkaido, Japan: Evidence for dehydration embrittlement as a cause of intraslab earthquakes, *Gondwana Research*, *16*, 470-481.

Park S.-C., and J. Mori (2008), Rupture velocity estimation of large deep-focus earthquakes surrounding Japan, *J. Geophys. Res., 113*, B08303,

doi:10.1029/2007JB005434.

Peacock, S. M. (2001), Are the lower planes of double seismic zones caused by serpentine dehydration in subducting oceanic mantle?, *Geology, 29*, 299-302.

Peyrat, S. and P. Favreau (2010), Kinematic and spontaneous rupture models of the 2005 Tarapaca intermediate depth earthquake, *Geophys. J. Int., 181*, 369-381, doi:10.1111/j.1365-246X.2009.04493.x.

Peyrat, S., K. B. Olsen, and R. Madariaga (2004), Which dynamic rupture parameters can be estimated from strong ground motion and geodetic data?, *Pure and Applied Geophys., 161*, 2155-2169.

Peyrat, S., J. Campos, J. B. de Chabalier, A. Perez, S. Bonvalot, M.-P. Bouin, D. Legrand, A. Nercessian, O. Charade, G. Patau, E. Clevede, E. Kausel, P. Bernard, and J.-P. Vilotte (2006), Tarapaca intermediate-depth earthquake (M_W 7.7, 2005, northern Chile): A slab-pull event with horizontal fault plane constrained from seismologic and geodetic observations, *Geophys. Res. Lett., 33*, L22308, doi:10.1029/2006GL027710.

Raleigh, C. B., and M. S. Paterson (1965), Experimental deformation of serpentinite and its tectonic implications, *J. Geophsy. Res., 70*, 3965-3985.

Rietbrock, A., and F. Waldhauser (2004), A narrowly spaced double-seismic zone in the subducting Nazca plate, *Geophys. Res. Lett., 31*, L10608, doi:10.1029/2004GL019610.

Sibson, R. H. (1977), Kinetic shear resistance, fluid pressures and radiation efficiency during seismic faulting, *Pure and Applied Geophys., 115*, 387-400.

Takahashi, M., K. Mizoguchi, and K. Masuda (2009), Potential of phyllosilicate dehydration and dehydroxylation reactions to trigger earthquakes, *J. Geophys. Res., 114*, B02207, doi:10.1029/2008JB005630.

Tibi, R., G., Bock, and C. H. Estabrook (2002), Seismic body wave constraint on mechanisms of intermediate-depth earthquakes, *J. Geophys. Res., 107 (B3)*, 2047, doi:10.1029/2001JB000361.

Tsuji, Y., J. Nakajima, and A. Hasegawa (2008), Tomographic evidence for hydrated oceanic crust of the Pacific slab beneath northeastern Japan: Implications for water transportation in subduction zones, *Geophys. Res. Lett., 35*, L14308, doi:10.1029/2008GL034461.

Urata, Y., K. Kuge, and Y. Kase (2008), Heterogeneous rupture on homogenous faults: Three-dimensional spontaneous rupture simulations with thermal pressurization, *Geophys. Res. Lett., 35*, L21307, doi:10.1029/2008GL035577.

Venkataraman, A., and H. Kanamori (2004a), Effect of directivity on estimates of

radiated seismic energy, *J. Geophys. Res., 109*, B04301, doi:10.1029/2003JB002548.

Venkataraman, A., and H. Kanamori (2004b), Observational constraints on the fracture energy of subduction zone earthquakes, *J. Geophys. Res., 109*, B05302, doi:10.1029/2003JB002549.

Wada, I., and K. Wang (2009), Common depth of slab-mantle decoupling: Reconciling diversity and uniformity of subduction zones, *Geochem. Geophys. Geosyst., 10*, Q10009, doi:10.1029/2009GC002570.

Wang, K. (2002), Unbending combined with dehydration embrittlement as a cause for double and triple seismic zones, *Geophys. Res. Lett., 29*, 1889, doi:10.1029/2002GL015441.

Wang, R. (1999), A simple orthonormalization method for stable and efficient computation of Green's functions, *Bull. Seismo. Soc. Amer., 89*, 733-741.

Warren, L. M., A. N. Hughes, and P. G. Silver (2007), Earthquake mechanics and deformation in the Tonga-Kermadec subduction zone from fault plane orientations of intermediate- and deep-focus earthquakes, *J. Geophys. Res., 112*, B05314, doi:10.1029/2006JB004677.

Warren, L. M., M. A. Langstaff, and P. G. Silver (2008), Fault plane orientations of intermediate-depth earthquakes in the Middle America Trench, *J. Geophys. Res., 113*, B01304, doi:10.1029/2007JB005028.

Warren, L. M., and P. M. Shearer (2002), Mapping lateral variations in upper mantle attenuation by stacking P and PP spectra, *J. Geophys. Res., 107 (B12)*, 2342, doi:10.1029/2001JB001195.

Wessel, P., and W. H. F. Smith (1998), New, improved version of the Generic Mapping Tools released, *EOS Trans. AGU, 79*, 579.

Yamasaki, T., and T. Seno (2003), Double seismic zone and dehydration embrittlement of the subducting slab, *J. Geophys. Res., 108 (B4)*, 2212, doi:10.1029/2002JB001918.

Yuan, X., S.V. Sobolev, R. Kind, O.Oncken, G. Bock, G. Asch, B. Schurr, F. Graeber, A. Rudloff, W. Hanka, K. Wylegalla, R. Tibi, Ch. Haberland, A. Rietbrock, P. Giese, P. Wigger, P. Rower, G. Zandt, S. Beck, T. Wallace, M. Pardo, and D. Comte (2000), Subduction and collision processes in the Central Andes constrained by converted seismic phases, *Nature, 408*, 958-961.

Figure Captions

Figure 1. Seismicity in northern Chile during the period from 1976 through 2008. (a) Map view of Global CMT solutions. The arrow indicates the motion of the Nazca plate relative to the South American plate [NUVEL-1A; DeMets et al., 1994]. (b) East-west cross section of seismicity. Earthquakes in the region between 19° S and 21° S are plotted with NEIC depths. The star indicates the hypocenter of the 2005 Tarapaca earthquake. (c) T (diamonds) and P (crosses) axes of Global CMT solutions in the region between 19° S and 21° S. The axes are projected on a lower hemisphere. (d) Number (N) of earthquakes as a function of NEIC depth. Earthquakes range from 15° S to 25° S.

Figure 2. Locations of five regional stations used in this study (triangles). The star indicates the epicenter of the 2005 Tarapaca mainshock. Gray dots correspond to aftershocks within a week of the mainshock. Hypocenter data are from NEIC.

Figure 3. Displacement waveforms recorded at the station PICA. (a) The mainshock and (b) an aftershock (19.99° S 68.81° W depth 105km M_W 5.6, NEIC) eight days after the mainshock. Original accelerograms are integrated with respect to time, and filtered with a pass band between 0.05 and 0.2 Hz.

Figure 4. Teleseismic P and pP displacement waveforms as a function of station azimuth. P and pP waveforms are vertical components, band-pass filtered between 0.02 and 1 Hz. The waveforms are aligned by the times of initial motions. The amplitudes are normalized by the maximum in each trace. (a) Observations. On the right-hand side of each trace, distance (degrees) and station name are shown. The gray traces were not used to compute correlation coefficients in Table 3. Only waveforms of pP to the east are used in this study because pP waves toward the west are close to a P-wave nodal plane. (b) Synthetic waveforms of the kinematic source model that was determined with the velocity model of Delouis and Legrand [2007] and the hypocenter relocated from the arrival-time dataset of 5 P and 3 S (5P3S).

Figure 5. Moment tensor solutions obtained from regional waveforms for seven sets of the velocity model and hypocenter. The velocity models are the two local models of Delouis and Legrand [2007] (DL07) and Peyrat et al. [2006] (P06), and a global model *iasp91*. Hypocenters are classified by three datasets of arrival times used for the

relocation (5P5S, 5P3S, and 3P3S). For the point-source moment tensor solutions, three components of band-passed filtered displacement waveforms were inverted. The pass band is between 0.03 and 0.1 Hz, except for ARIE which used 0.04 and 0.1 Hz. We used these low-cut frequencies for the stable waveforms. Green functions were computed with the method of Wang [1999]. The inversion method is the same as Kuge [2003]. The source time function is assumed to be a Herrmann function [Herrmann, 1979] with a duration of 18.5 s that was derived from the empirical relation between duration and magnitude [Kikuchi and Ishida, 1993]. In each case, source depth was examined in a grid search technique, and the optimal depth was in a range from 100 to 120 km.

Figure 6. Final slip distributions of the kinematic finite-fault source models obtained from regional waveforms. The models were obtained for seven sets of the velocity model and hypocenter. The velocity models and hypocenter classifications are the same as in Figure 5. Contours are drawn at intervals of 2 m. Stars indicate the hypocenter. For the source models, three components of displacement waveforms were modeled in a multiple time window technique [Hartzell and Heaton, 1983; Kuge, 2003]. The waveforms were bandpass-filtered with a high-cut frequency of 0.2 Hz and the same low-cut frequency as for the moment tensor inversions. The value in the lower-left corner of each panel indicates variance reduction, which shows how well the observed waveforms are modeled with synthetics [Kuge, 2003]. A larger value of variance reduction corresponds to better waveform modeling, and 100% means that observed and synthetic waveforms are completely the same. A gray rectangle in the solution of the DL07 velocity model and 5P3S hypocenter indicates the region used to determine our dynamic source model.

Figure 7. Snap shots of slip propagation in a kinematic finite-fault source model obtained from regional waveforms. For the source model, the velocity model DL07 [Delouis and Legrand, 2007] was used along with the hypocenter relocated from the arrival-time dataset of five P and three S (5P3S). Contours of slip are drawn at intervals of 2 m. Stars indicate the hypocenter.

Figure 8. Comparison between observed and synthetic waveforms at regional stations for the solutions shown in Figures 7 and 12. Thick solid curves are the observed displacement waveforms. Thin solid and dashed curves indicate the synthetic waveforms of the kinematic and dynamic source models, respectively. All traces are displayed on the same scale. The dynamic source model was inferred from the

kinematic source model.

Figure 9. Comparison of four observed and synthetic teleseismic P and pP waveforms. Thick and thin lines indicate observed and synthetic waveforms, respectively. For the synthetic waveform labels, the initial “d-“ or “p-“ represents the kinematic source models derived with the velocity models of Delouis and Legrand [2007] or Peyrat et al. [2006], respectively, and the following text (i.e. 3P3S, 5P3S, or 5P5S) indicates the arrival-time dataset used in hypocenter relocation for the source model.

Figure 10. Values of seismic radiation energy as a function of station azimuth. Black and gray circles indicate the values of the 2005 Tarapaca and 1993 Kushiro earthquakes, respectively. Each data point corresponds to a value obtained from a single station.

Figure 11. Dynamic source model inferred from the kinematic source model. (a) Slip-weakening relation used in this study, and obtained distributions of (b) strength excess (MPa) and (c) dynamic stress drop (MPa). The contours are drawn at intervals of 25 MPa. Negative stress drop which is shown by the gray region is allowed in this study. The considered rectangular fault is shown in Figure 6. The determination technique is based on Mikumo and Miyatake [1993] and Mikumo et al. [1998]. In the 3-D numerical computation of dynamic rupture, the grid spacing is 0.25 km, and the sampling time interval is 0.0125 s. The initial stress is uniform. Dynamic ruptures are calculated in the same method as Kase and Kuge [2001], except that an infinite medium is assumed because of the deep source region of the Tarapaca earthquake. P and S wave velocities and density are the same as those in the source depth of the kinematic source model. The kinematic model was determined using the velocity model of Delouis and Legrand [2007] and the hypocenter relocated from the dataset of 5P3S.

Figure 12. (a) Snap shots of slip propagation and (b) distribution of final slip from the dynamic source model in Figure 11. The considered rectangular fault is shown in Figure 6. Contours of slip are drawn at intervals of 2 m. Stars indicate the hypocenter.

Figure 13. (a) Rupture characteristics of the 2005 Tarapaca earthquake. (b) Conceptual model in the east-west cross section to explain the rupture characteristics. The thick black lines correspond to the two patches of large slip and high stress drop.

Figure 14. Schematic illustration for predicted effect of pore pressure p on a

slip-weakening relation. TP denotes thermal pressurization. The change in pore pressure due to thermal pressurization is Δp. Pore pressure affects effective normal stress $\sigma_n^{eff} = \sigma_n - p$, where σ_n is normal stress. Shear stress τ on a fault varies with slip Δu as follows:

$$\tau = \begin{cases} \mu_s \sigma_n^{eff} - (\mu_s \sigma_n^{eff} - \mu_d \sigma_n^{eff}) \Delta u / D_c & \Delta u < D_c \\ \mu_d \sigma_n^{eff} & \Delta u \geq D_c \end{cases},$$

where μ_s is the static friction coefficient, μ_d is the dynamic friction coefficient, and D_c is the critical distance. The shear stress values, τ_s and τ_d, correspond to $\mu_s \sigma_n$ and $\mu_d \sigma_n$, respectively.

Figure 15. Numerical simulation of 3-D spontaneous dynamic rupture on a rectangular fault with heterogeneous fluid distribution. (a) Model. In the gray regions, fluid exists causing thermal pressurization. (b) Slip evolution on the fault in meters. (c) Slip-weakening curves at three sites on the fault which are indicated by the diamonds in (a). The initial and normal stresses are 60 and 85 MPa, respectively. The static friction coefficient is 0.8, and the dynamic friction coefficients in the initial crack and in the other regions are 0.588 and 0.73, respectively. P and S wave velocities and density are the same as those for the dynamic source model in Figure 11. The shear zone thickness is 2 cm. The hydraulic diffusivity is 0.02 m^2/s. The time step is 0.00075 s. The other parameters are the same as those in Bizzarri and Cocco [2006]. The computation method is the same as Urata et al. [2008].

Tables

Table 1. Hypocenters relocated in this study.

Velocity model	Used arrival times	Latitude (°N)	Longitude (°E)	Depth (km)
DL07	5P5S	-20.07	-69.39	113.5
	5P3S	-20.03	-69.28	110.0
	3P3S	-20.00	-69.23	106.3
P06	5P5S	-20.08	-69.41	114.2
	5P3S	-20.02	-69.30	109.1
iasp91	5P5S	-20.08	-69.40	110.7
	5P3S	-20.01	-69.29	105.9
NEIC	NEIC	-19.99	-69.20	115
DL07	DL07	-20.01	-69.24	108
P06	P06	-20.168	-69.264	97.6

P06 and DL07 denote Peyrat et al. [2006] and Delouis and Legrand [2007], respectively. 5P5S means that arrival times of five P and five S from the five stations in Figure 2 were used. 5P3S means that arrival times of five P and three S were used by excluding two S of CALA and TCP from 5P5S. 3P3S means that arrival times of three P and three S from ARIE, IQUI, and PICA were used. The three lines at the bottom indicate the hypocenters of NEIC, Peyrat et al. [2006], and Delouis and Legrand [2007].

Table 2. Best double-couple parameters of the moment tensor solutions.

Velocity model	Used arrival times	Strike (°)	Dip (°)	Rake (°)
DL07	5P5S	183	19	-77
	5P3S	187	23	-73
	3P3S	180	23	-82
P06	5P5S	179	24	-76
	5P3S	188	30	-69
iasp91	5P5S	173	20	-86
	5P3S	178	24	-81
GCMT	GCMT	182	23	-81

DL07	DL07	175	15	-90
P06	P06	189	24	-74

Strike angles are measured clockwise from the north. DL07, P06, 5P5S, 5P3S, and 3P3S are the same denotations as those in Table 1. The three lines at the bottom indicate the parameters given by Global CMT (GCMT), Peyrat et al. [2006] (P06), and Delouis and Legrand [2007] (DL07).

Table 3. Correlation coefficients computed for observed teleseismic P and pP waveforms.

	Hypocenter Relocation Data		
Velocity Model	5P5S	5P3S	3P3S
DL07	0.93	0.93	0.92
P06	0.92	0.86	-
iasp91	0.91	0.91	-

DL07, P06, 5P5S, 5P3S, and 3P3S are the same as in Table 1. Correlation coefficients for the seven source models are given. A dash indicates no results for the case. The correlation coefficient is computed by

$$\frac{\sum_j \sum_i \frac{1}{c_j^2} x^j(t_i) s^j(t_i - \Delta t^j)}{\sqrt{\sum_j \sum_i \frac{1}{c_j^2} x^j(t_i)^2} \sqrt{\sum_j \sum_i \frac{1}{c_j^2} s^j(t_i)^2}},$$

where $x^j(t_i)$ and $s^j(t_i)$ are observed and synthetic waveforms of *j-th* trace at time t_i, respectively. c_j is the maximum amplitude of observed waveform of *j-th* trace. Δt^j is chosen so that correlation coefficient for *j-th* trace can be maximized.

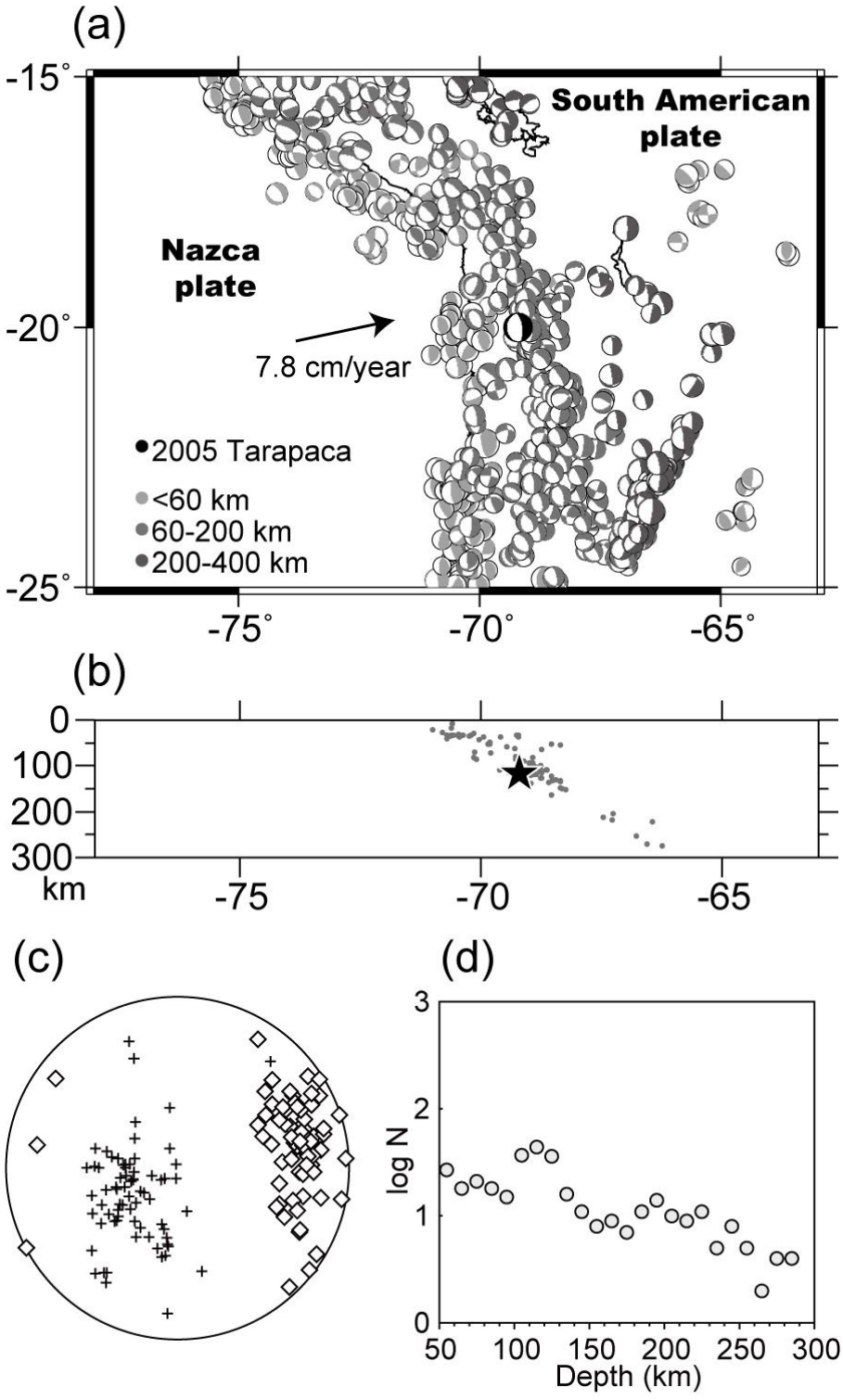
(a)
-15˚
-20˚
-25˚
-75˚
-70˚
-65˚
South American plate
Nazca plate
7.8 cm/year
2005 Tarapaca
<60 km
60-200 km
200-400 km
(b)
0
100
200
300
km
-75
-70
-65
(c)
(d)
log N
Depth (km)
0
1
2
3
50
100
150
200
250
300

Figure 1

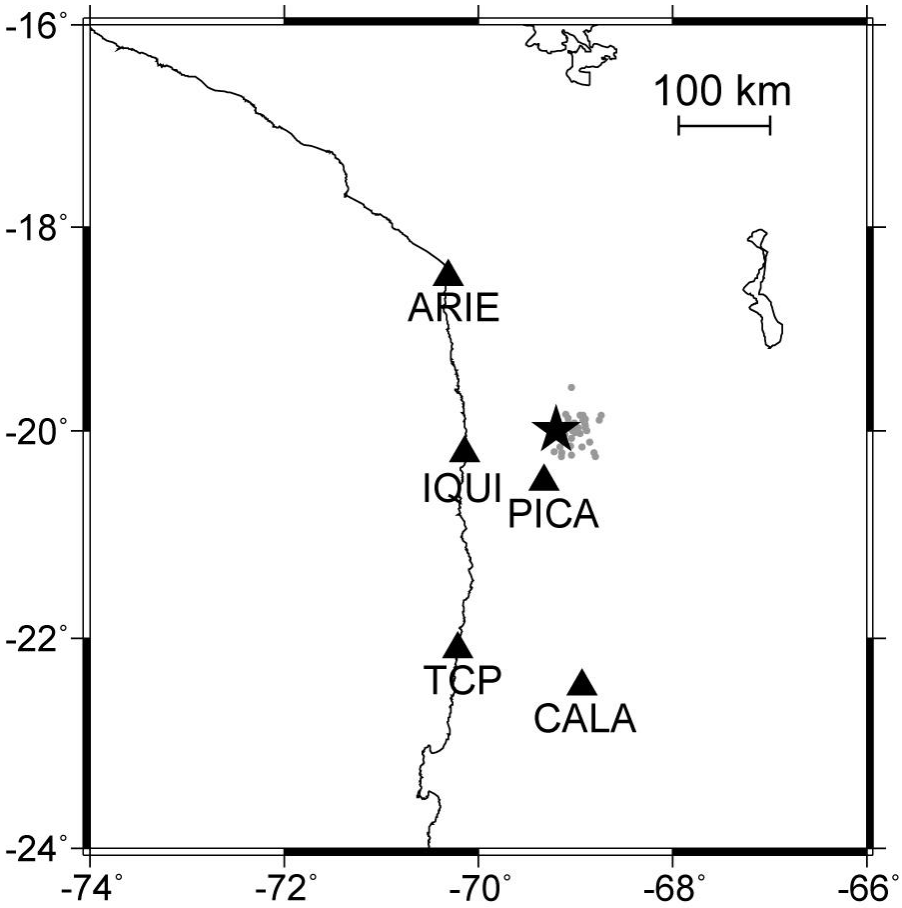

Figure 2

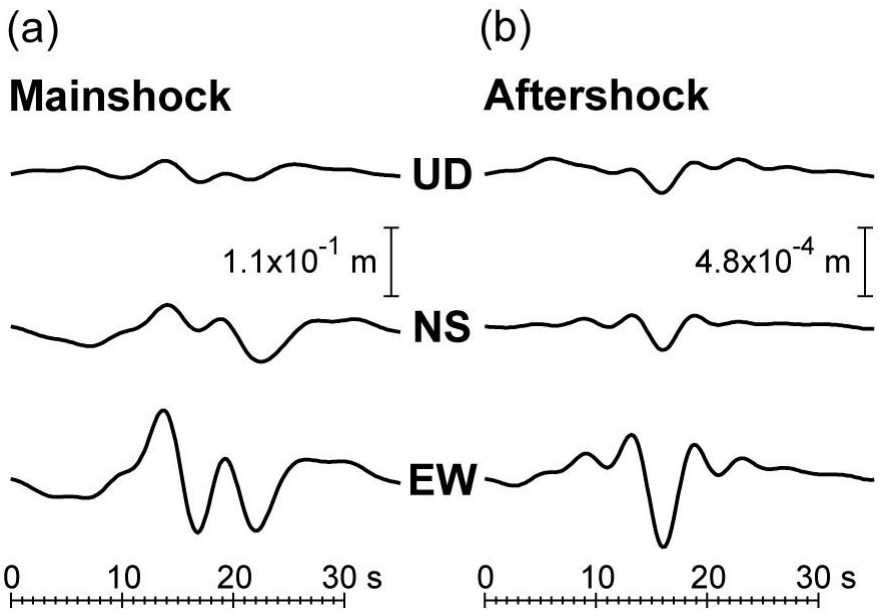
(a)
Mainshock
(b)
Aftershock
UD
1.1x10-1 m
4.8x10-4 m
NS
EW
0
10
20
30 s
0
10
20
30 s

Figure 3

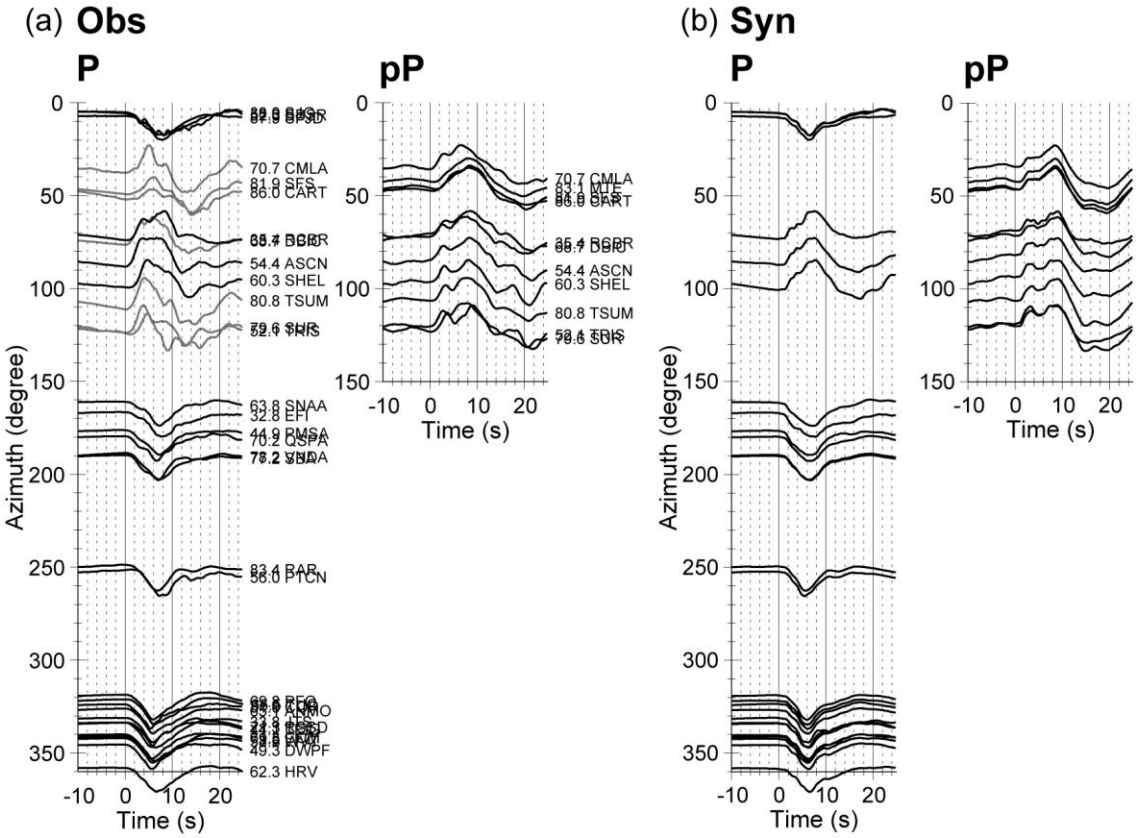
(a) Obs
P
pP
(b) Syn
P
pP
Azimuth (degree)
Time (s)
70.7 CMLA
81.9 SES
86.0 CART
54.4 ASCN
60.3 SHEL
80.8 TSUM
63.8 SNAA
32.8 EFI
70.2 QSPA
83.4 BAR
56.0 PTCN
49.3 DWPF
62.3 HRV

Figure 4

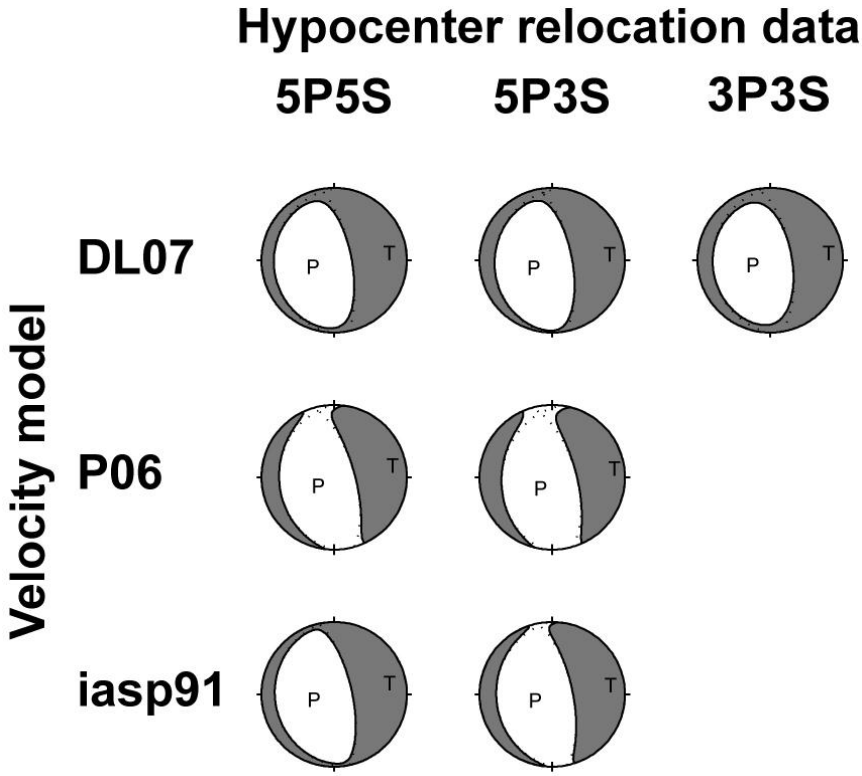
Hypocenter relocation data
5P5S
5P3S
3P3S
Velocity model
DL07
P06
iasp91
P
T

Figure 5

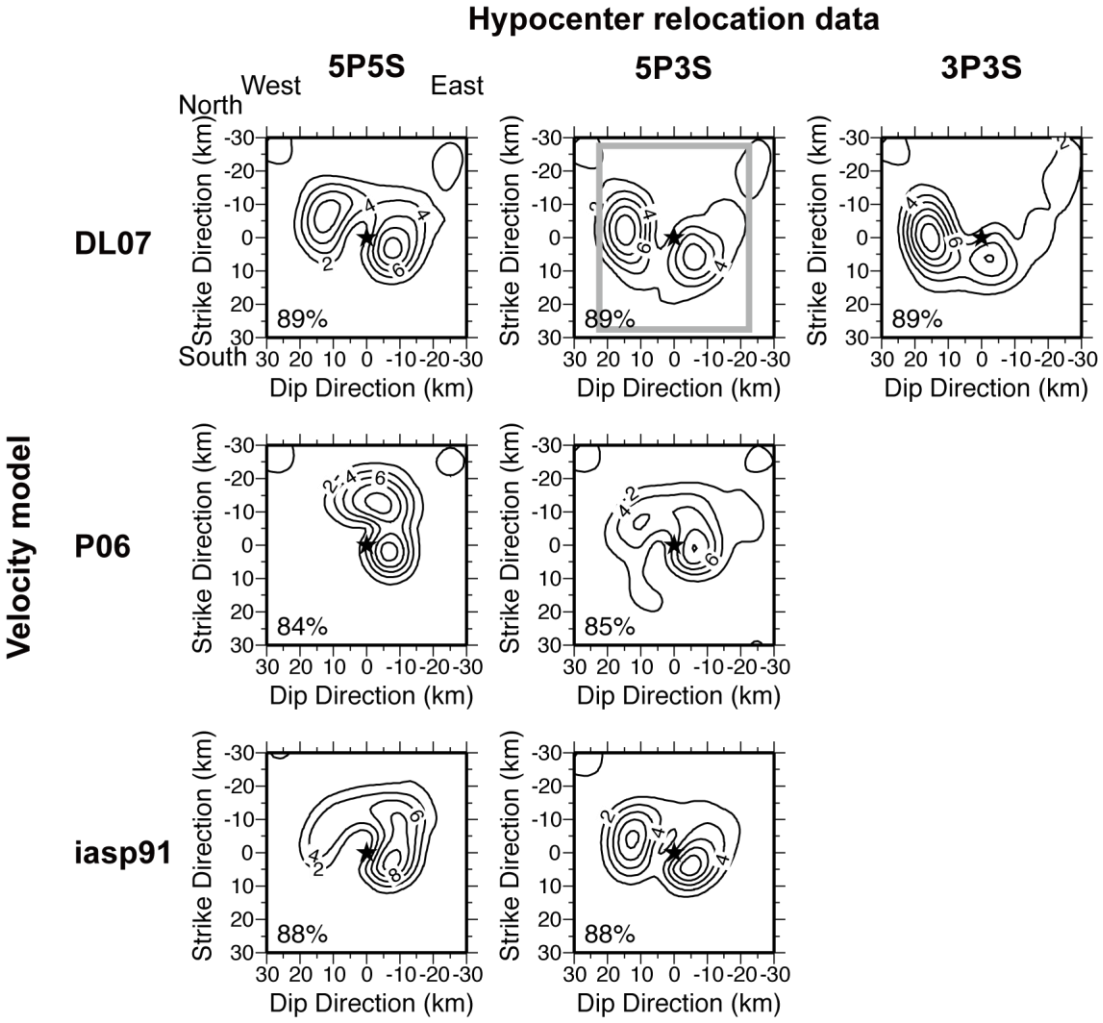
Hypocenter relocation data
5P5S
5P3S
3P3S
West
East
North
South
Velocity model
DL07
P06
iasp91
Strike Direction (km)
Dip Direction (km)
89%
89%
89%
84%
85%
88%
88%

Figure 6

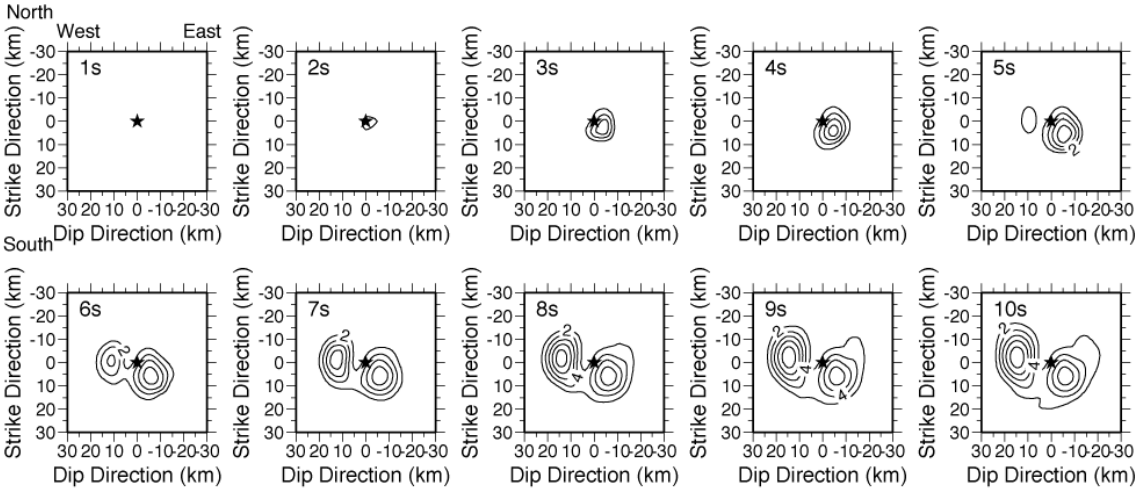
North
West
East
South
1s
2s
3s
4s
5s
6s
7s
8s
9s
10s
Strike Direction (km)
Dip Direction (km)
-30 -20 -10 0 10 20 30
30 20 10 0 -10 -20 -30
2
4

Figure 7

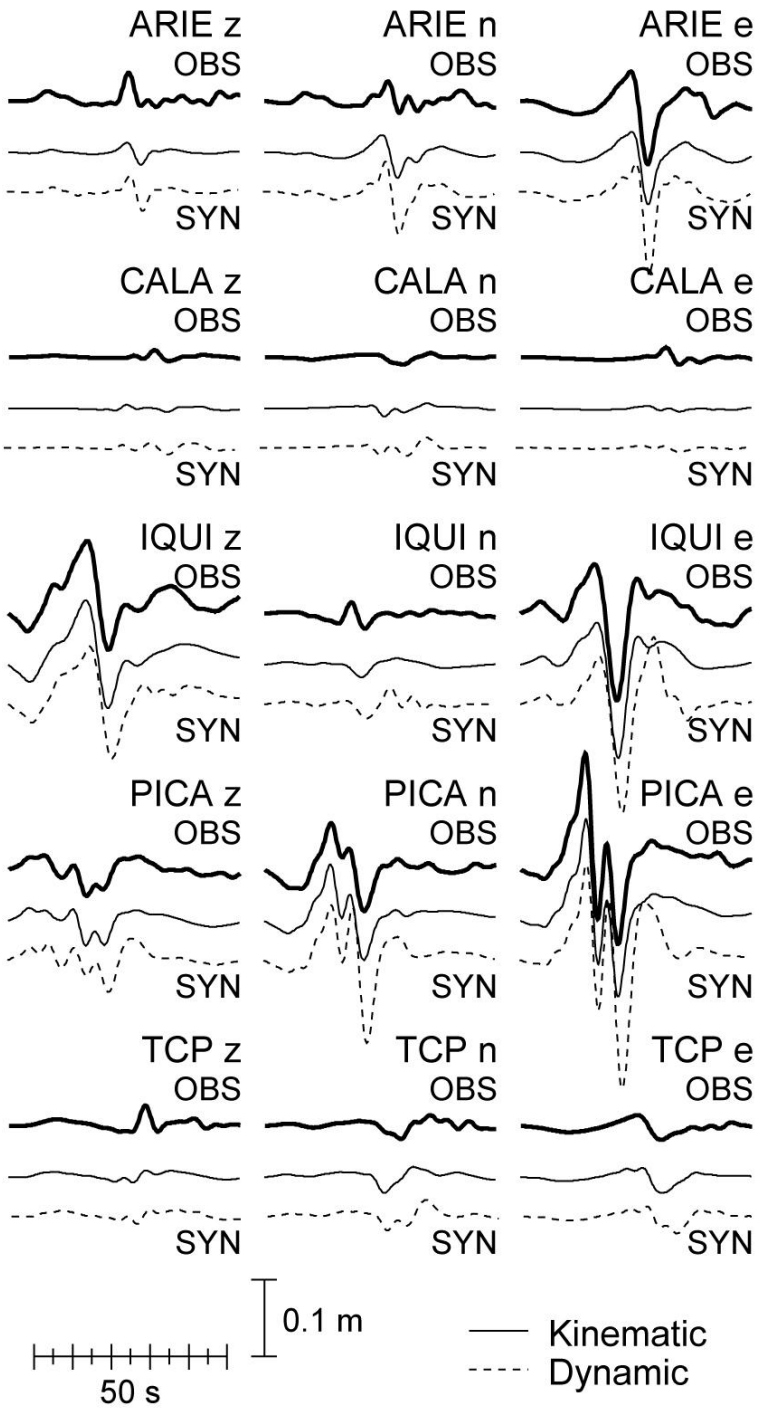
ARIE z
OBS
SYN
ARIE n
OBS
SYN
ARIE e
OBS
SYN
CALA z
OBS
SYN
CALA n
OBS
SYN
CALA e
OBS
SYN
IQUI z
OBS
SYN
IQUI n
OBS
SYN
IQUI e
OBS
SYN
PICA z
OBS
SYN
PICA n
OBS
SYN
PICA e
OBS
SYN
TCP z
OBS
SYN
TCP n
OBS
SYN
TCP e
OBS
SYN
0.1 m
50 s
Kinematic
Dynamic

Figure 8

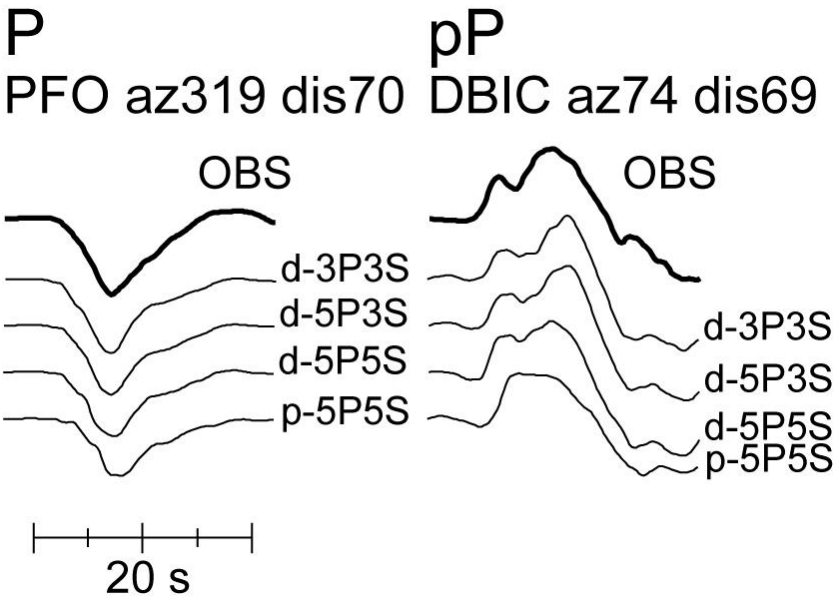
P
PFO az319 dis70
OBS
d-3P3S
d-5P3S
d-5P5S
p-5P5S
20 s
pP
DBIC az74 dis69
OBS
d-3P3S
d-5P3S
d-5P5S
p-5P5S

Figure 9

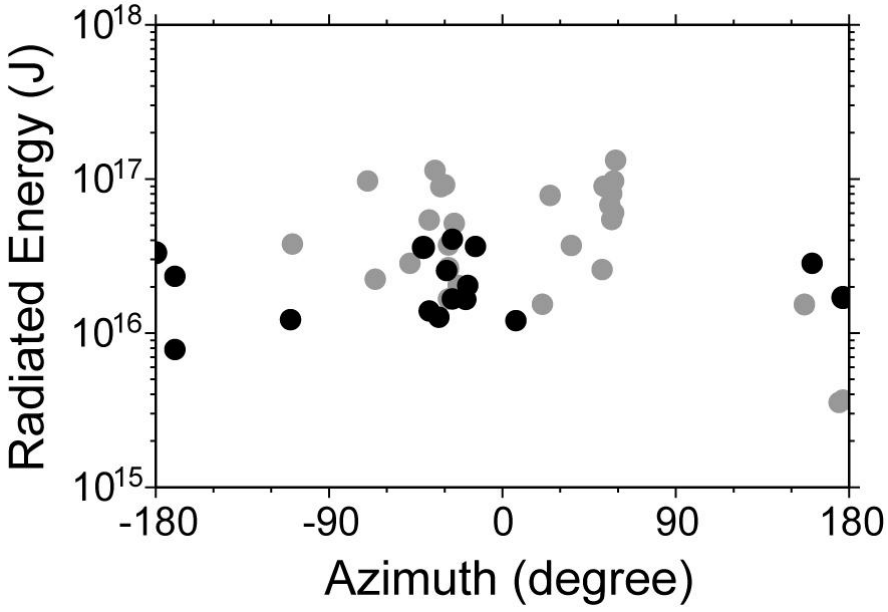
Radiated Energy (J)
10^18
10^17
10^16
10^15
-180
-90
0
90
180
Azimuth (degree)

Figure 10

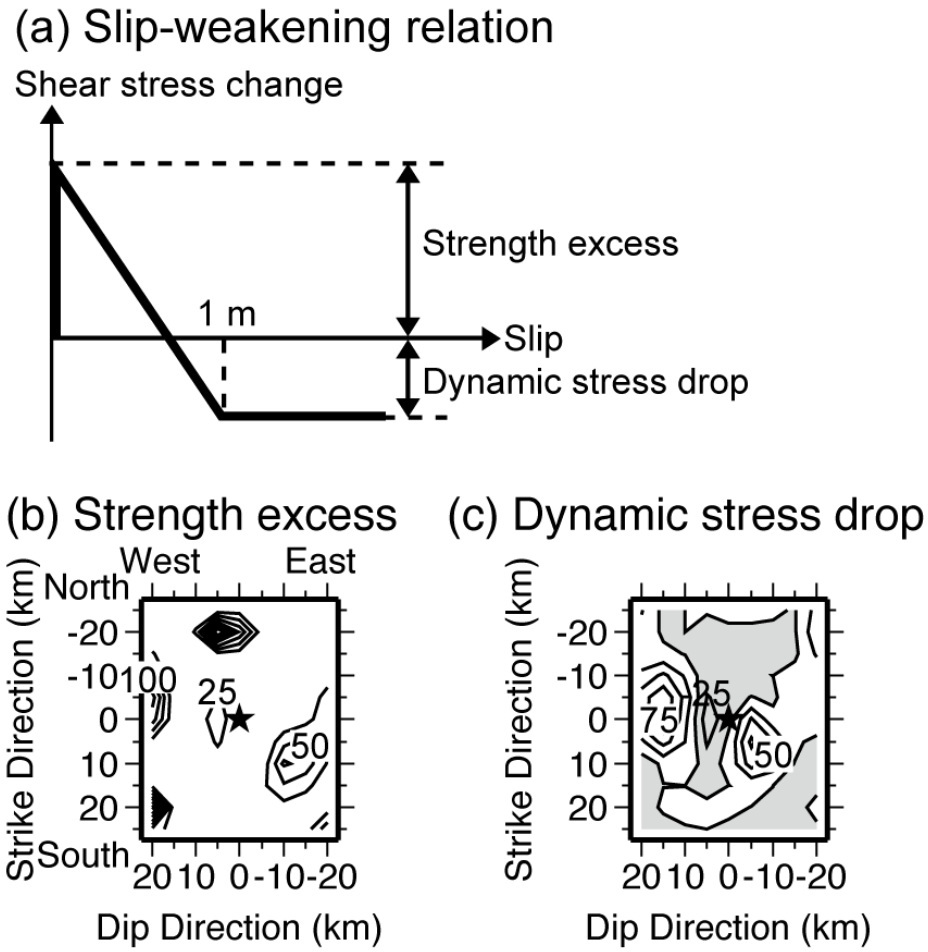
(a) Slip-weakening relation
Shear stress change
Strength excess
1 m
Slip
Dynamic stress drop
(b) Strength excess
(c) Dynamic stress drop
West
East
North
South
Strike Direction (km)
Dip Direction (km)
-20
-10
0
10
20
25
50
75
100
20 10 0 -10 -20

Figure 11

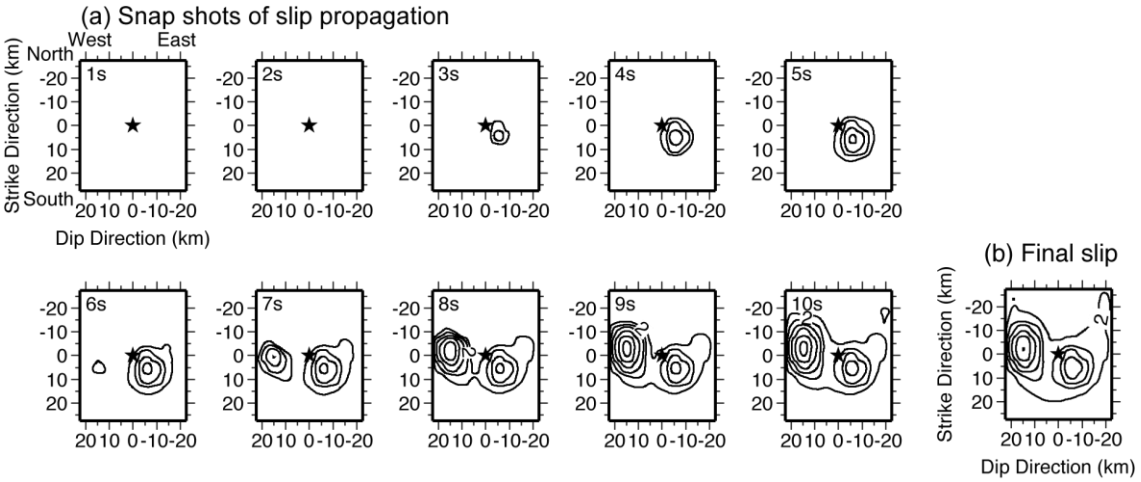
(a) Snap shots of slip propagation
West
East
North
South
Strike Direction (km)
Dip Direction (km)
1s
2s
3s
4s
5s
6s
7s
8s
9s
10s
(b) Final slip
Strike Direction (km)
Dip Direction (km)

Figure 12

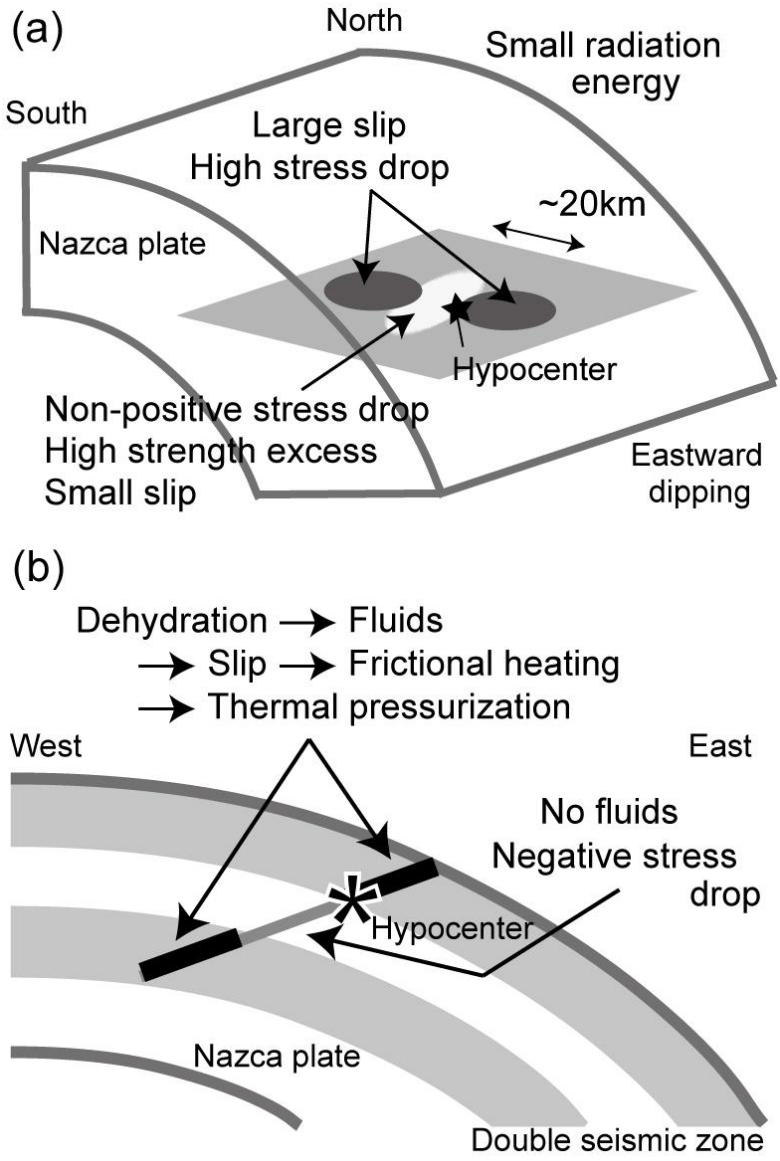
(a)
North
Small radiation energy
South
Large slip
High stress drop
~20km
Nazca plate
Hypocenter
Non-positive stress drop
High strength excess
Small slip
Eastward dipping
(b)
Dehydration → Fluids
→ Slip → Frictional heating
→ Thermal pressurization
West
East
No fluids
Negative stress drop
Hypocenter
Nazca plate
Double seismic zone

Figure 13

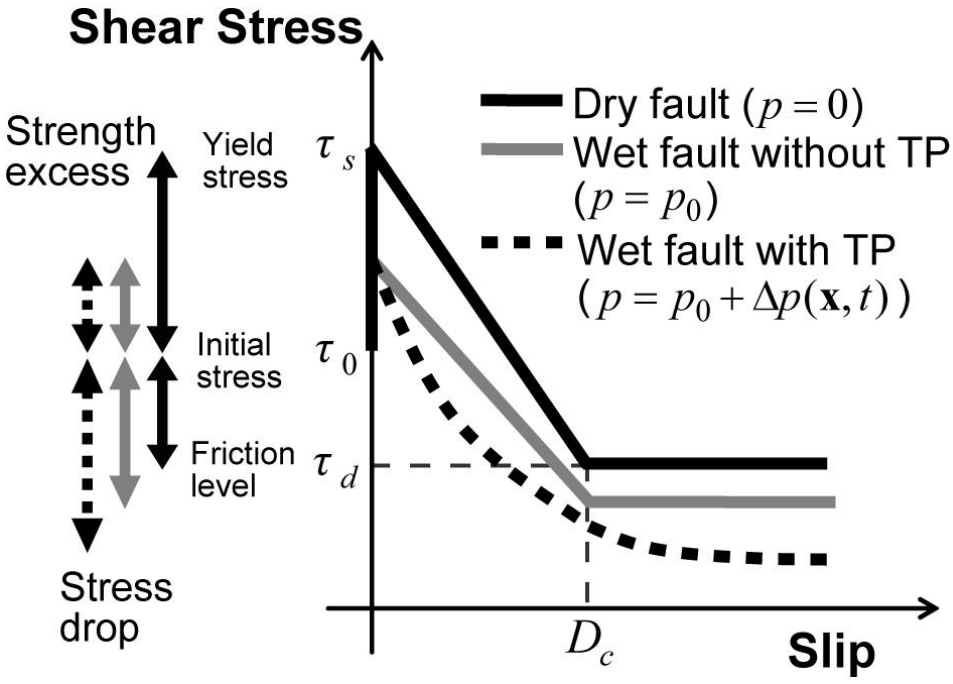
Shear Stress
Strength excess
Yield stress
Initial stress
Friction level
Stress drop
τ_s
τ_0
τ_d
D_c
Slip
Dry fault ($p = 0$)
Wet fault without TP ($p = p_0$)
Wet fault with TP ($p = p_0 + \Delta p(\mathbf{x}, t)$)

Figure 14

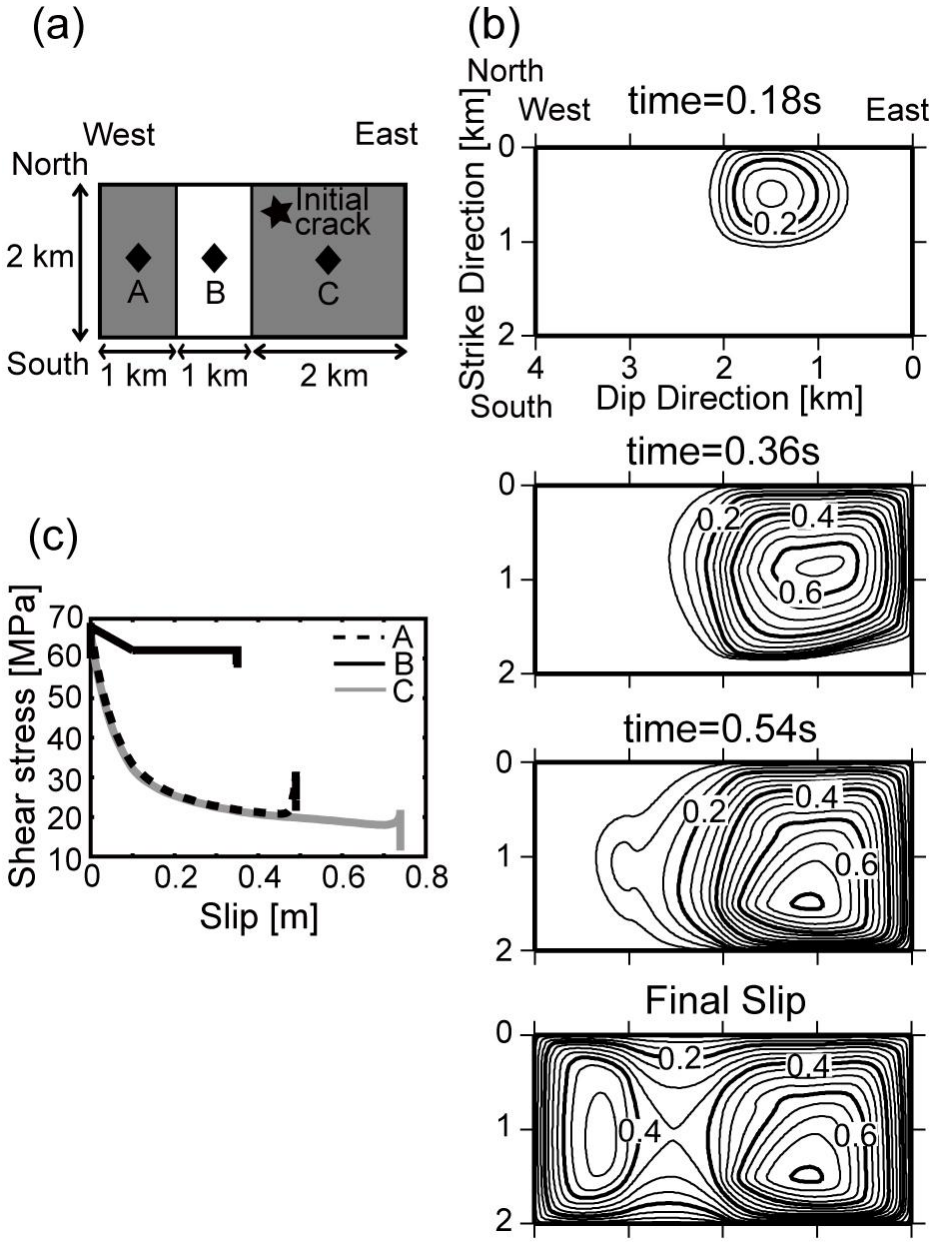
(a)
West
East
North
2 km
Initial crack
A
B
C
South
1 km
1 km
2 km
(b)
North
West
time=0.18s
East
Strike Direction [km]
0.2
South
Dip Direction [km]
time=0.36s
0.2
0.4
0.6
time=0.54s
0.2
0.4
0.6
Final Slip
0.2
0.4
0.4
0.6
(c)
Shear stress [MPa]
A
B
C
Slip [m]

Figure 15